AUTHOR(S)	Aye, M. M., Rivasto, E., Zhao, Y., Huhtinen, H., & Paturi, P.
TITLE	Enhanced current-carrying capability in YBCO coated conductor bilayers for high-field applications
YEAR	2024
DOI	10.1088/1402-4896/ad5a4e
CITATION	Aye, M. M., Rivasto, E., Zhao, Y., Huhtinen, H., & Paturi, P. (2024). Enhanced current-carrying capability in YBCO coated conductor bilayers for high-field applications. Physica Scripta, 99(8), 085901. https://doi.org/10.1088/1402-4896/ad5a4e
VERSION	Accepted Manuscript
LICENSE	© This version has been published under A Creative Commons Attribution-NonCommercial-NoDerivatives 4.0 International (CC BY-NC-ND 4.0) license ; https://creativecommons.org/licenses/by-nc-nd/4.0/deed.en

Enhanced current-carrying capability in YBCO coated conductor bilayers for high-field applications

M. M. Aye[1,2], **E. Rivasto**[1], **Y. Zhao**[3], **H. Huhtinen**[1] **and P. Paturi**[1]

[1] Wihuri Physical Laboratory, Department of Physics and Astronomy, FI-20014 University of Turku, Finland

[2] University of Turku Graduate School (UTUGS), University of Turku, FI-20014 Turku, Finland

[3] School of Electronic Information and Electrical Engineering, Shanghai Jiao Tong University, 200240 Shanghai, People's Republic of China

E-mail: `petriina.paturi@utu.fi`

Abstract.

We have investigated the impact of bilayer structures on the critical current density, J_c, of $\mathrm{YBa_2Cu_3O_{6+x}}$ (YBCO) coated conductor films, *i.e.* films grown on buffered metal substrates, under varying temperature and magnetic field conditions. The bilayers consisted of a YBCO layer free of artificial pinning centers and 8 wt.% $\mathrm{BaZrO_3}$-added (BZO) layer on top, where the thickness percentage of the layers was varied from 0 to 100 %. The results reveal that the bilayer configuration enhances J_c at temperatures below 60 K, with a significant improvement in high magnetic fields (5–8 T) and temperatures ≤ 20 K. The optimal BZO-added layer thickness was found to be approximately 70 %, reaching 80 % at 8 T. Structural examinations indicate improved growth of YBCO and BZO nanorods in the bilayer structure with BZO-added layer thickness ≤ 80 %. Theoretical model of the bilayer structure considering the layers as two parallel superconductors with different properties was developed. It was found that the model adequately explains all the experimentally observed tendencies, and thus the observed maximum in J_c is due to better growth of the BZO-added layer. The study provides valuable insights for designing optimal bilayer structures for diverse applications operating in different temperature and magnetic field regimes.

1. Introduction

High critical current coated conductors (CCs) have become a reality today, and their application in various power devices relies on the improvement of vortex pinning capabilities, especially at high magnetic fields and temperatures [1–4]. Critical current density J_c is a fundamental superconducting property influenced not only by intrinsic parameters like critical temperature T_c and electronic structure but also by extrinsic vortex pinning mechanisms associated with microscopic defects within the superconductor matrix [5–9].

Extrinsic vortex pinning, such as nanoscale artificial pinning centers (APCs), offers an effective solution for pinning quantized magnetic vortices in high-temperature superconductors (HTSs), particularly $YBa_2Cu_3O_{6+x}$ (YBCO) films and coated conductors [10–13]. This enhancement of J_c is essential for the practical use of HTS electrical power application. However, a challenge in this research lies in addressing the reduction in self-field critical current density $J_c(0)$ when artificial pinning centers are introduced into HTS. The presence of significant strain not only affects the growth of the mixed morphologies of APCs, but it also deteriorates the superconducting properties, *e.g.* $J_c(0)$, of the YBCO matrix [8, 14], causing a significant obstacle in practical HTS applications. When striving to optimize J_c at high magnetic fields, achieving the best possible combination between $J_c(0)$ and in-field $J_c(B)$ is essential [4, 5, 15].

Notably, various multilayered structures, such as YBCO/YBCO-BZO [16–18], YBCO-BZO/YBCO-Y_2O_3 [19], Y_2O_3/YBCO [20], YBCO-BZO/ CeO_2 [17, 18], YBCO-BZO /YBCO-$BaSnO_3$ [21], YBCO-BZO /YBCO-$BaCeO_3$ [22], YBCO-4wt%BZO / YBCO-12wt%BZO [23] and various other combinations [24] have demonstrated substantial improvements in YBCO microstructure, current-carrying capabilities, and pinning in YBCO films of larger thickness, offering one solution to produce the high enough J_c level. In addition, thin seed layers have been used to improve the growth of the YBCO layer. Using a 50 nm APC-free SmBCO layer below BHO-added layer enabled growth at lower temperature [25, 26] improving the crystal growth of the BHO-added layer. Other typical seed layers are Y_2O_3 [27–29] as a layer of the buffer stack. On the other hand, a systematic study on the effect of the seed layer thickness seems to be lacking. In chemical solution deposition methods, seed layers are needed [30] to ensure the proper growth of the film. Recent theoretical and experimental results observed in [31–33] confirm that the performance of conventional HTS films can be greatly enhanced by using bilayers based on YBCO/YBCO+BZO heterostructures on single crystalline STO substrates. The bilayer structure, consisting of approximately 30% YBCO and 70% YBCO+6wt% BZO, was found to be optimal across a wide range of magnetic fields and temperatures, resulting in an almost 60% increase in the critical current density compared to single layer films.

For a coated conductor technology, bilayers have the potential to be a significant advancement due to its effectiveness and more simple manufacturing process than needed for multilayers. However, films grown on buffered metal substrates typically

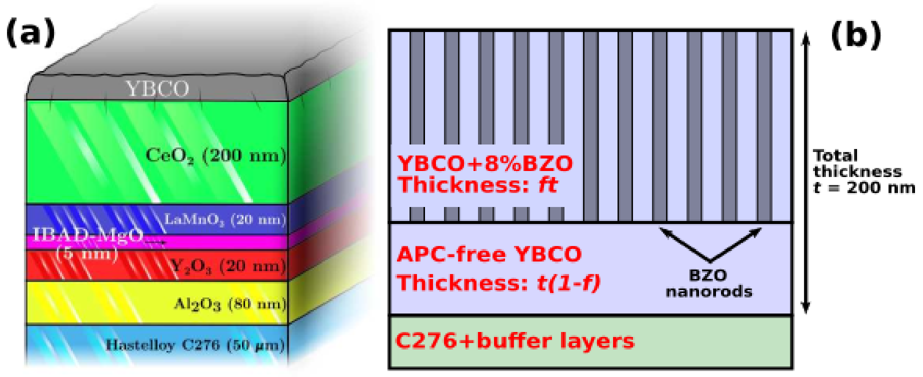

Figure 1. (a) A metallic Hastelloy C276 substrate accompanied by an advanced buffer layer structure. The grey YBCO layer on top represents either the APC-free or 8 wt.% BZO-added YBCO single layer, or a bilayer combination of the two. (b) A schematic representation of the investigated bilayer YBCO films, where the ratio between the thicknesses of the APC-free layer next to the substrate (pale blue: APC-free YBCO layer) and the BZO-added YBCO layer forming nanorod network on top varies (pale blue: APC-free YBCO surrounding, dark grey: columnar structure of BZO nanorods). The parameter f denotes the percentage of the BZO-added layer in relation to the total film thickness t; for instance, $f = 00$ indicates 0%, $f = 01$ indicates 10%, and $f = 10$ represents 100% BZO-added YBCO, respectively.

contain significantly more crystalline defects than films on single crystals and thus the conclusions of [31–33] cannot automatically be assumed to hold. Therefore, in this study, we deposited bilayer structures on a buffered metal Hastelloy C276 substrate. These structures consisted of varying thicknesses of APC-free and BZO-added YBCO layers. This was done to cater to the needs of different practical applications that operate within a wide range of magnetic fields and temperatures. We conducted structural and magnetic characterizations of these multilayers and compare and discuss the results in relation to YBCO and BZO-added YBCO single layer films.

2. Experimental details

A set of bilayer structures consisting of APC-free YBCO bottom layer and 8 wt.% BZO-added YBCO layer on the top was fabricated by pulsed laser deposition (PLD) on buffered metal hastelloy C276 with an advanced Al_2O_3/Y_2O_3/IBAD-MgO/$LaMnO_3/CeO_2$ buffer layer [34]. Additionally, as a comparison, single layer films were deposited using both compositions. The thicknesses of the layers were adjusted to change the percentage thickness of the BZO-added layer, denoted as f, relative to the total film thickness (approximately 200 nm as determined individually for each sample by atomic force microscopy measurements over the etched stripe). This change ranged from 0% to 100% in 10% increments, corresponding to samples $f = 00$, $f = 01$, $f = 02$, $f = 03$, $f = 04$, $f = 05$, $f = 06$, $f = 07$, $f = 08$, $f = 09$, and $f = 10$, as schematically depicted in Fig. 1. Additional details about the growth process and deposition parameters can be

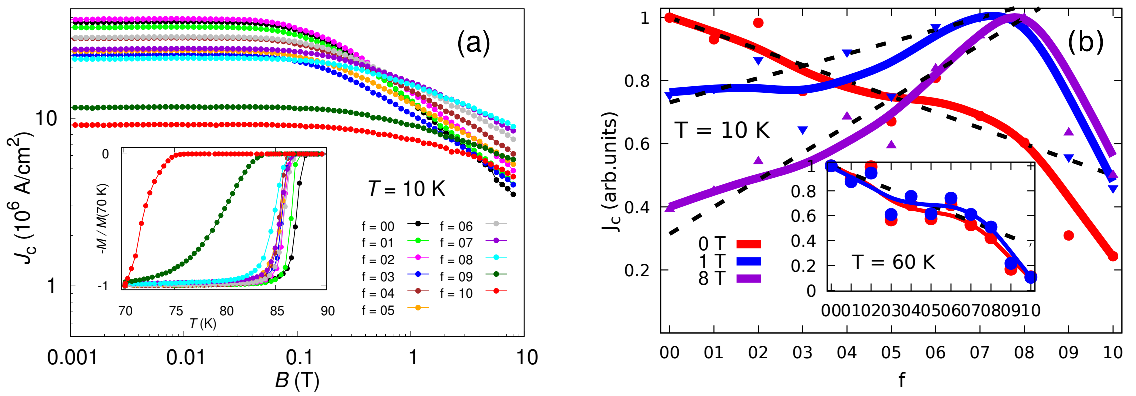

Figure 2. (a) In the main panel, an example of magnetic field dependencies of J_c is displayed, determined from the opening of the magnetic hysteresis loop measured at 10 K for various f values representing different bilayer combinations. The inset illustrates the normalized ac magnetization variation with temperature, showing how the T_c decreases with increasing f. (b) Scaled and smoothed curves describing the alteration in the maximum critical current density value with changing layer ratio f in the YBCO bilayer structure. At low temperatures below 50 K (main panel), a maximum in-field J_c occurs in the $f = 06$–08 range, while at temperatures above 50 K (inset), the APC-free YBCO sample exhibits the highest J_c across all magnetic field ranges. The black dashed lines are the calculated theoretical values discussed in subsection 3.3.

found in our previous works [35, 36].

The crystallographic properties of the films were analyzed using x-ray diffraction (XRD) with a PANalytical Empyrean diffractometer operated in Bragg-Brentano mode. High-resolution transmission electron microscopy (HRTEM) was conducted using a JEOL JEM-2200FS electron microscope equipped with a 200 kV field emission gun (FEG) and in-column energy filter (Omega filter). Additionally, a probe-corrected scanning transmission electron microscopy (STEM) employing high-angle annular dark-field imaging (HAADF STEM) was carried out using the Titan 80-300 microscope operating at 200 kV.

Magnetic analysis was conducted using a Quantum Design PPMS system. The critical temperatures were determined from the AC magnetization curves, and the critical current densities were calculated by analyzing the openings of the hysteresis loops, employing the Bean model for rectangular films [37]. The accommodation field B^*, defined as the upper limit of the low-field plateau of $J_c(B)$, was determined using the criterion $J_c(B)/J_c(0) = 0.9$ [38].

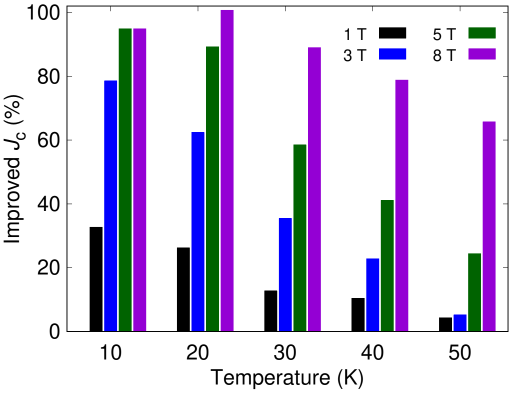

Figure 3. Enhancement of in-field J_c in the YBCO bilayer structure compared to the J_c value of the best single layer film, measured at various temperature and magnetic field ranges. The optimal in-field J_c is consistently achieved with bilayer ratios in the range $f = 06$–08. However, this improved in-field J_c is not observed at temperatures exceeding 50 K, and the self-field $J_\mathrm{c}(0)$ at all temperatures remains highest in the APC-free single layer YBCO film.

3. Results and discussion

3.1. Temperature and magnetic field dependent enhancement of J_c

The superconducting critical temperatures, T_c, of the films were determined through ac susceptibility measurements. Inset of Fig. 2(a) illustrates that T_c decreases and the transition broadens as the BZO layer thickness f increases. Notably, the single APC-free layer exhibits the highest onset T_c, approximately ≈ 88 K. However, the decrease T_c is moderate until f exceeds 08, when T_c starts to decrease significantly.

To further illustrate, we have presented raw magnetic field-dependent critical current density $J_\mathrm{c}(B)$ data measured at 10 K in the main panel of Fig. 2(a). It clearly shows that self-field $J_\mathrm{c}(0)$ decreases as f increases, while high-field J_c increases as the BZO-added layer becomes thicker with higher f. The absolute values of $J_\mathrm{c}(0) > 40$ MA/cm^2 at 10 K are on par with the state-of-the-art [39]. In Fig. 2(b), we have provided scaled and smoothed curves to demonstrate how the maximum J_c shifts to a different f range in various magnetic field ranges. In self-field and at low temperatures, J_c decreases nearly linearly with increasing f, while in a wide magnetic field range of 1–8 T, J_c has a maximum value at a BZO layer thickness of approximately $f = 07$. Upon closer examination, it is evident that the maximum point of the J_c curves shifts slightly to higher values of f, such as $f = 08$ at 8 T. This behaviour is consistent across all temperatures below 50 K. However, above this temperature, the bilayer structure no longer enhances J_c, and the APC-free single layer structure consistently yields the highest J_c in all field ranges, as depicted in the inset of Fig. 2(b).

In Fig. 3, we present a comprehensive overview of the enhancements in J_c achieved across various temperature and magnetic field ranges due to bilayering. Firstly,

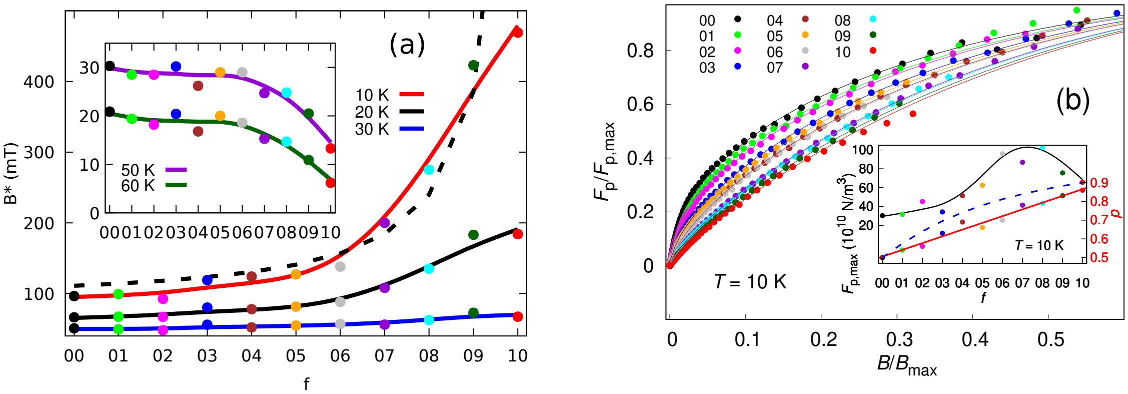

Figure 4. (a) The bilayer thickness ratio f dependent accommodation field B^* measured at different temperatures. (b) The magnetic field dependent pinning force data fitted to Eq. (1) for various bilayer structures with different f values. The inset shows the maximum pinning force $F_{\mathrm{p,max}}$ determined from the scaled pinning force function $F_{\mathrm{p}}/F_{\mathrm{p,max}}$ fitted at 10 K and the linear increase in the actual flux pinning exponent p with increasing f. The black (a) and blue (b) dashed lines are the calculated theoretical values discussed in subsection 3.3.

it is evident that the increase in J_{c} through bilayer structures is only observed at temperatures below 60 K, with no improvement in the self-field region. Consequently, the bilayer's efficacy becomes particularly pronounced at high magnetic fields, where enhancements of over 90% in J_{c} are realized within the 5–8 T range and at low temperatures ≤ 20 K. On average, the most favorable layer ratio appears to be $f = 07$, although at the highest field strength of 8 T, the maximum improvement is attained at $f = 08$. In summary, the insights provided in Fig. 3 can serve as a valuable reference when evaluating the optimal bilayer structure for diverse applications operating within different temperature and magnetic field regimes.

In order to comprehend the roles played by the APC-free layer and the BZO-added YBCO layer in enhancing the in-field J_{c} of the bilayer structure, we delved into the f-dependent flux pinning properties. As illustrated in the main panel of Fig. 4(a), the low-field plateau of $J_{\mathrm{c}}(B)$, and consequently B^*, remains nearly constant up to $f = 05$. Beyond this point, a rapid increase is observed, and this effect is notably more prominent at lower temperatures. Conversely, at higher temperatures ($T \geq 50$ K), B^* starts to decline as f exceeds 05. This decline is closely associated with the bilayer structure's efficacy, which, as previously demonstrated, is only pronounced below 50 K, corresponding to the improved J_{c} capacity (as seen in the inset of Fig. 4(a)).

To dissect the actual flux pinning effects and isolate the contribution of $J_{\mathrm{c}}(0)$, which consistently plays a pivotal role in the absolute $J_{\mathrm{c}}(B)$ value, we conducted a meticulous examination of the shapes of the $J_{\mathrm{c}}(B)$ curves above B^*. Initially, we derived the scaled pinning force function $F_{\mathrm{p}}/F_{\mathrm{p,max}}$ using the formula $F_{\mathrm{p}}(B) = BJ_{\mathrm{c}}(B)$ (Fig. 4(b)). This

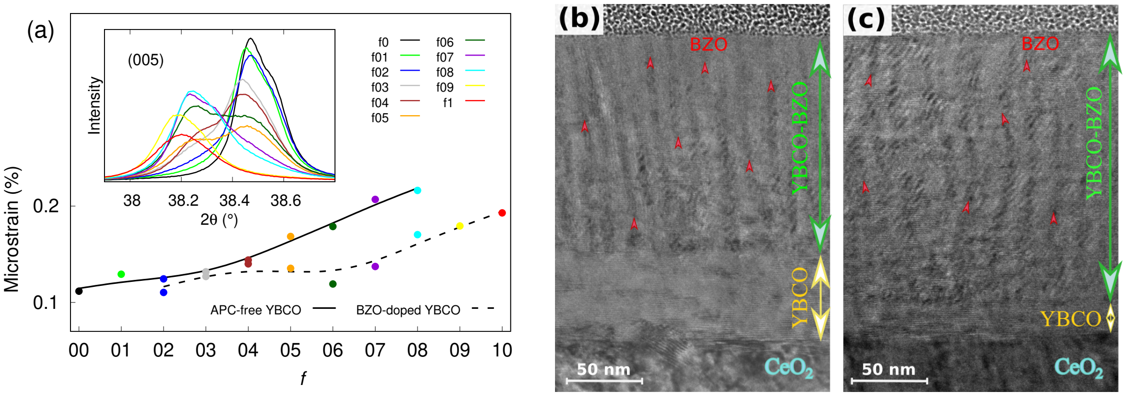

Figure 5. (a) The non-uniform microstrain values were determined through Williamson-Hall analysis of XRD peaks in films with varying thickness ratios between the APC-free YBCO layer adjacent to the substrate interface (solid line) and the 8% BZO-added YBCO layer on top (dashed line). The inset illustrates the evolution of the XRD 2θ (005) peak, where each sample exhibits two components corresponding to the different thicknesses of the aforementioned layers. (b)–(c) Cross-sectional HRTEM images of samples $f = 07$ and $f = 09$, respectively. The APC-free YBCO layer is positioned next to the CeO_2 buffer layer interface at the bottom, with the layer of 8% BZO-added YBCO situated on top. The red arrowheads highlight the presence of BZO nanorods within the YBCO matrix.

enabled us to express the formula in its more-reliable-to-fit form [40–42]

$$\frac{F_{\mathrm{p}}(B)}{F_{\mathrm{p,max}}} = \frac{(p+q)^{p-1}p^q}{q^q}\left(\frac{B}{B_{\mathrm{max}}}\right)^p\left(\frac{p+q}{p} - \frac{B}{B_{\mathrm{max}}}\right)^q. \qquad (1)$$

Here, $F_{\mathrm{p,max}}$ and B_{max} are the value and field of the $F_{\mathrm{p}}(B)$ curve maximum, and usually within the measured range. In addition we fit p and q, which are linked to the size and number of the pinning centers, along with their impact on the vortex lattice. The parameter q had been previously determined to be very close to the value of 1.1 [42]. As such, we have presented the parameters $F_{\mathrm{p,max}}$ and p in Fig. 4(b). As observed, the exponent p related to flux pinning increases linearly with the increasing f, and this enhancement is notably more conspicuous below 50 K. Conversely, $F_{\mathrm{p,max}}$ reaches its maximum value around $f = 07$, closely mirroring the trends in the in-field $J_{\mathrm{c}}(B)$ at lower temperatures. This unequivocally signifies that the absolute $J_{\mathrm{c}}(B)$ is contingent not solely on flux pinning but is also influenced by the self-field $J_{\mathrm{c}}(0)$ and, thus, the combined layers, or more precisely, the crystallographic quality of the APC-free YBCO in these layers, holds paramount significance in this regard.

3.2. Improved growth of YBCO and BZO nanorods in bilayer structures

The structural properties of the deposited films were carefully examined through XRD θ–2θ, ω, and 2D (θ–ϕ) scans to gain insights into their crystalline phase, presence of impurities, as well as in-plane and out-of-plane quality. The results obtained from XRD θ–2θ scans unveiled that all the deposited films displayed epitaxial texture, characterized by prominent $(00l)$ peaks of the YBCO phase and an additional BZO (200) peak at $2\theta \approx 43.3^\circ$ in bilayer films.

To assess the structural differences between deposited bilayer films and single layer YBCO films without APCs ($f = 00$) and with APCs ($f = 10$), the details of the (005) Enhanceddiffraction peak structure were investigated and the results are shown in Fig. 5. As can be seen, in bilayer films the (005) diffraction peaks revealed a two-peak structure. These peaks were situated around the corresponding peaks observed in single layer YBCO films without APCs and with APCs. To distinguish the components within bilayer films clearly, a deconvolution of the (005) diffraction peak was performed. It became evident that both components of APC-free and BZO-added YBCO layers were present in the bilayer films, with their relative intensity ratios closely following f. For instance, in films $f = 01$ and $f = 09$, each layer of BZO-added YBCO and APC-free YBCO appeared quite thin, making it challenging to discern respective layers with well-defined unit cell structures. In contrast, the respective peaks were clearly dominant when the layers were sufficiently thick.

The c-axis lattice parameters were determined from the (005) peaks of APC-free and BZO-added YBCO. Notably, the BZO-added YBCO layer exhibited a longer c lattice parameter, ranging from 11.75 Å to 11.78 Å, in comparison to the APC-free YBCO, which ranged from 11.69 Å to 11.72 Å. In both layers, c is slightly increased with increasing f, and the most significant elongation was formed in $f = 01$, $f = 09$ and $f = 10$. These results suggest that lattice strain could be substantial when the layer is not thick enough to accommodate the growth of YBCO, as seen in films $f = 01$ and $f = 09$. Moreover, lattice strain appeared more pronounced when the film included APCs, which elevate significant strain due to lattice mismatch, particularly in the $f = 10$ film. However, the full width at half maximum (FWHM) of the (005) peaks produced by BZO-added YBCO was consistently lower compared to APC-free YBCO layers, especially in the range from $f = 06$ to $f = 09$. These results implied a reduction in non-uniform strain within the YBCO matrix of the BZO-added YBCO layer.

To confirm the presence of microstrain in our bilayer films, a comprehensive strain analysis was carried out using the Williamson-Hall method, and the outcomes are illustrated in Fig. 5. Generally, the results indicated a consistent increase in microstrain as the f is increased, most notably above $f = 06$. This intriguing behaviour strongly suggests a significant relaxation of strain and an enhancement in in-plane coherence within bilayer films. In terms of in-plane quality, 2D (θ–ϕ) scans of the YBCO (102) peak and BZO (110) peak provided assurance that there was no systematic variation in the in-plane direction for both YBCO and BZO, even as the layer thickness of the bilayer film changed. However, the most significant variation was observed in the out-of-plane direction, analyzed through the (005) rocking curves along the ω-direction. The narrowest peak width along the ω-direction for both YBCO and BZO indicated a substantial improvement in long-range lattice ordering in the out-of-plane direction, particularly in film $f = 07$.

In summary, when taking into account microstrain relaxation and out-of-plane coherence, it becomes evident that the optimal bilayer film appears to be situated within the parameter range of $f = 06$ to $f = 08$. The observed decrease in microstrain within this specific range and the enhancement in out-of-plane coherence signify a delicate balance that has been achieved, underlining the importance of precise control of layer thickness and composition for tailored structural properties.

To gain insights into how the BZO phase disperses within the YBCO matrix and the defect associated with dopant structures in the bilayer films, we conducted a scanning transmission electron microscopy (STEM) study. Fig. 5(b) and (c) represent the cross-sectional STEM images of bilayer films for $f = 07$ and $f = 09$ configurations. As seen in figures, both films exhibit two distinct layers, one composed of APC-free material and the other induced by APC, and they were clearly visible. The APC-induced layers in both films have thicknesses of $\approx 140\,\mathrm{nm}$ for $f = 07$ and $\approx 180\,\mathrm{nm}$ for $f = 09$, while the APC-free YBCO layer is $\approx 60\,\mathrm{nm}$ thick in $f = 07$ and $\approx 20\,\mathrm{nm}$ in $f = 09$. In the APC-induced layer, we observed well-aligned BZO nanorods that extended vertically throughout the film's thickness. These nanorods had a diameter of $\approx 6\,\mathrm{nm}$ and were spaced about $\approx 8\,\mathrm{nm}$ apart in both the $f = 07$ and $f = 09$ films. In the $f = 07$ film (see Fig. 5(b)), the boundary between the two layers was sharply defined, showing the perfect growth of BZO nanorods starting from the interface. There was no evidence of strain region at the interface, and the BZO nanorods exhibited steady, straight growth, forming continuous nanorods on top of the APC-free layer. Consequently, the nanorods reach a length of roughly matching the thickness of the entire APC-induced layer. In contrast, the $f = 09$ film exhibited a different growth mode for both the YBCO and BZO nanorods, as depicted in Fig. 5(c). At the interface, a strained region is evident, causing the vertically aligned nanorods to deviate from their ideal growth direction. Additionally, the average length of the nanorods experiences a significant reduction in the $f = 09$ configuration. Moreover, we observed local lattice distortion, indicative of the tilting growth of the BZO nanorods in the film. Compared to the $f = 07$ film, where the tilt angle was $\approx 3°$, the tilting growth of the nanorods varied from 3 to 15° in the $f = 09$ film. The average length of the nanorods reduced to about half of the thickness of the APC-induced layer. This tilting growth is likely a result of the substantial strain between the APC-induced and APC-free interfaces. The first layer produced by APC-free material appears to be insufficiently thick to provide a strain-free surface for BZO growth. As YBCO competes with BZO during the initial film growth, it may be challenging for BZO to grow laterally and achieve the width necessary for domain matching epitaxy. Furthermore, structural defects, such as stacking faults and dislocations resulting from strain relaxation, might contribute to the reduction in nanorod length. This tilting growth also had an impact on the local out-of-plane and in-plane lattice relationships.

Thus, TEM investigations of as-grown bilayer samples clearly reveal a correlation between the critical thickness of the respective layers and microstructural features in multilayered film design. These microstructural features are instrumental in understanding and tailoring the physical and superconducting properties of YBCO high-temperature superconductors, particularly the self-field and in-field critical current density of these compounds.

3.3. Modelling $J_c(f, B, T)$

As a simple null hypothesis theoretical model of the bilayers, we can assume the double layer as consisting of the APC-free (Y) and APC-induced (BZO) layers and assume that the physical properties of the layers do not change from these end values and that the layers do not interact. Then we can take the experimental values for the layers and calculate what should happen in case of two parallel conductors with relative thicknesses described by f. The critical current density scales linearly with f as

$$J_{\mathrm{c,tot}} = J_{\mathrm{c,Y}}(B,T)(1-f) + J_{\mathrm{c,BZO}}(B,T)f, \tag{2}$$

as can be deduced by considering the current paths in the parallel configuration. J_c for both parts of the multilayer is determined as

$$J_{\mathrm{c,(Y|BZO)}}(B,T) = \min\left(J_{\mathrm{c,0}}(T), J_{\mathrm{c,v}}(T,B)\right), \tag{3}$$

where $J_{\mathrm{c,0}}$ is the field independent zero-field value, which depends on the crystal quality of the film [43], and $J_{\mathrm{c,v}}$ is the vortex pinning dependent part at high applied field, which depends mostly on the pinning centers. At zero applied field $J_c(T) = J_{\mathrm{c,0}}(T)$ and it can be taken directly from the experiments. The temperature dependence of $J_{\mathrm{c,0}}(T)$ was found to decrease exponentially as

$$J_{\mathrm{c,0}}(T) = J_{\mathrm{c,0}}(0\,\mathrm{K})\exp(-T/T_0) \tag{4}$$

for both APC-free ($f = 00$) and APC-added ($f = 10$) samples with T_0 equal to 35.5 K and 30 K, respectively. This fitted dependence was used in all the following calculations. Clearly, since $J_{\mathrm{c,Y}}(0\,\mathrm{T}) > J_{\mathrm{c,BZO}}(0\,\mathrm{T})$, $J_{\mathrm{c,tot}}$ should linearly decrease with f, as seen in Fig. 2b with the experimental red line and the theoretical black dashed line.

The pinning part of J_c, requires a bit more work, but the overall shape of the curve is well described by the Dew-Hughes equation Eq. (1) where $F_{\mathrm{p,max}}$, B_{max} and p can be taken from the experimental values of the single layer films. The temperature dependence of the parameters was also fitted with the data using decreasing exponential functions similar to Eq. 4. Since in the used geometry $F_p = BJ_c$, F_p should also clearly increase linearly with f at 10 K, as is seen in the inset of Fig. 4(b) for samples where $f \leq 0.8$. In Fig. 2(b) are shown the calculated relative J_c values (black dashed lines) as function of f at magnetic fields of 0 T, 1 T and 8 T at 10 K and 60 K, overlaid with the experimental data. It is clear that the main features are present in this simple model: (1) decreasing $J_c(f)$ at 0 T, (2) increasing $J_c(f)$ at higher fields with the slope increasing with field, and (3) $J_c(f)$ decreases in all fields at 60 K. We will return to the experimentally observed, but not theoretically expected, maximum later.

Since the above calculations seem to reproduce the observed tendencies well, we can now easily calculate, for example, the accommodation field B^* as the crossing point of the $J_{\mathrm{c,0}}$ and $J_{\mathrm{c,v}}$. This calculation done at 10 K is shown as the black dashed line in

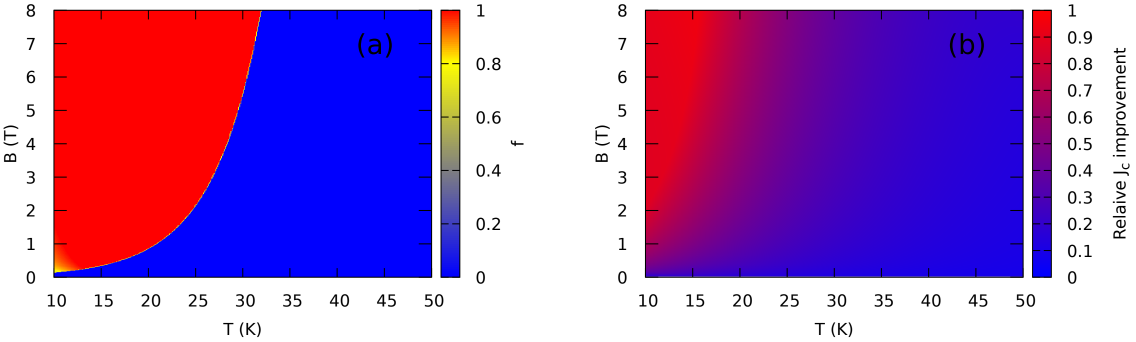

Figure 6. (a) Calculated optimal f for different temperatures and magnetic fields. Only at low temperature and field, the bilayer structure is better than single APC-free or APC-induced layers. (b) Calculated relative improvement of J_c of the $f = 08$ sample compared to higher J_c of either the APC-free or the APC-induced film.

Fig. 4(a). Thus also this more derivative characteristic parameter follows the observed tendency well. Next, we turn to p. The dependence of $p(f)$ is not simple and it is easiest to just fit the Dew-Hughes equation to the F_p values calculated from the weighted sum of J_c both layers (Eq. 2), using $p = 0.5$ and $p = 0.9$ for $f = 00$ and $f = 10$, respectively. We get the curve shown in the inset of Fig. 4(b). There is slight discrepancy here between the model and the experimental value dependencies. This can be partly due to experimental errors in determining p from the F_p curve at low temperatures. Especially, for high p values, finding the correct $F_{p,max}$ and B_{max} values is difficult. Overall, the both increase monotonously.

Thus, we can conclude that the simplest possible model for the bilayer structure explains all the superconducting features up to $f = 08$. Above that the growth of both parts of the film are clearly defective as can be seen from the diminished T_c (Fig. 2(a)), clearly nonlinear dependence of J_c (Fig. 2(b)) and above all from the clearly widened XRD peaks and disordered structure in TEM (Fig. 5), indicating much larger non-uniform strain and therefore lowered electron mean free path in the films, leading to deviation from the expected behaviour [43]. This kind of defective growth is the root cause of the maximum observed at low temperature in the experimental $J_c(f)$ curves in Fig. 2. On the other hand, at higher temperatures, there is no maximum as the APC-free layer acts as the main current carrying layer. Therefore, we can conclude that to great extent the bilayer works as two independent different superconductors in parallel and one of the main reasons for the very high improvements of J_c at low temperatures and fields is the improved growth of the BZO-added layer on top of the APC-free layer compared to growth on the bare substrate, similarly as in the use of seed layers for SmBCO [25].

We can now also use the model to calculate the optimal f for different operation temperatures and fields by calculating the J_c at different fields and temperatures for different values of f using Eq. 2 and the exponential temperature dependencies (Eq.

4) for the parameters. The optimal f is taken as the value that produces highest J_c at that temperature and field. This way we get the dependence shown in Fig. 6(a). It is clear that depending on temperature and field, the optimum is either the APC-free or APC-added sample, provided that it has the optimal growth that the $f = 08$ sample has in our set. Only at low fields and temperatures there are conditions where some other values of f are optimal. It should be noted that here the APC-free YBCO-layer does not act only as a seed layer, but in very large temperature and field range is the main current carrying layer, even though it greatly improves the growth the APC-added layer. In sample $f = 09$ the APC-free layer is still too thin and structurally flawed to enable optimal growth of the APC-added layer, leading to the observed maximum at $f = 08$. Fig. 6(a) can be used as a guideline for choosing the correct type of doping for each application. APC-free wires for high temperature, low field applications and well grown APC-added wires for high fields. An easy way of achieving good growth is to use an APC-free layer between the substrate buffer layers and the APC-added layer.

In order to understand the improvement of results seen in Fig. 3, we calculated the expected improvement J_c with the $f = 08$ sample compared to the fitted values of the single layer films calculated as described above (Fig. 6(b)). It is clearly seen that the expected improvement tendency is similar to that observed experimentally: The improvement increases with field, but the effect decreases with increasing temperature as was also observed experimentally (Fig. 3). We can therefore conclude that the simple two channel model adequately explains all the observed features of the bilayer systems. The main benefit of the bilayering comes from the clearly improved growth of the APC-induced layer on top of APC-free YBCO compared to the growth on top of the bare buffer stack.

4. Conclusions

We have studied the enhancement of J_c under varying temperature and magnetic field conditions in YBCO coated conductor bilayers. The findings suggest that bilayer structures offer improved J_c at temperatures below 60 K, particularly in high magnetic fields (5–8 T) and temperatures $\leq$ 20 K. The optimal BZO-layer share is identified as $f = 07$ on average, reaching $f = 08$ at 8 T, emphasizing the importance of precise layer control for tailored structural properties.

The flux pinning analysis reveals that the bilayer's efficacy in enhancing J_c is more pronounced below 50 K, emphasizing the role of flux pinning effects. Structural examinations indicate improved growth of YBCO and BZO nanorods in the bilayer structure in bilayers where $f \leq 08$. Microstructural features, including lattice parameters and strain analysis, further support the delicate balance achieved in the optimal bilayer structure. Theoretical model of the bilayer structure considering the layers as two parallel superconductors with different properties was developed. It was found that the model adequately explains all the experimentally observed tendencies, and thus the observed maximum in J_c at low temperatures is due to better growth of the BZO-added layer on top of the APC-free layer. Based on the findings in this work, an APC-free layer of at least 50 nm thickness is needed to improve the growth of the APC-added layer on buffered metal substrates. Also, in large temperature and field range the APC-free layer was found to act as the main current carrying layer, indicating that the bilayer structure f has to be optimized for the working conditions.

This study contributes to a deeper understanding of the factors influencing J_c in YBCO coated conductor bilayers and provides a basis for designing optimal bilayer structures for various applications operating in different temperature and magnetic field regimes. Overall, these insights are crucial for advancing the development and application of high-temperature superconductors in practical scenarios.

5. Acknowledgements

The Jenny and Antti Wihuri Foundation is acknowledged for financial support.

References

[1] Larbalestier D, Gurevich A, Feldmann D M and Polyanskii A 2001 *Nature* **414** 368–377

[2] Kang S, Goyal A, Li J, Gapud A A, Martin P M, Heatherly L, Thompson J R, Christen D K, List F A, Paranthaman M and Lee D F 2006 *Science* **311** 1911–1914

[3] Varanasi C V, Burke J, Brunke L, Wang H, Sumption M and Barnes P N 2007 *J. Appl. Phys.* **102** 063909:1–5

[4] Obradors X and Puig T 2014 *Supercond. Sci. Technol.* **27** 044003:1–17

[5] Blatter G, Feigel'man M, Geshkenbein V, Larkin A and Vinokur V 1994 *Rev. Mod. Phys.* **66** 1125–1388

[6] Long N J, Strickland N M and Talantsev E F 2007 *IEEE Trans. Appl. Supercond.* **17** 3684–3687

[7] Civale L, Maiorov B, Serquis A, Willis J O, Coulter J Y, Wang H, Jia Q X, Arendt P N, MacManus-Driscoll J L, Maley M P and Foltyn S R 2004 *Appl. Phys. Lett.* **84** 2121–2123

[8] Foltyn S R, Civale L, MacManus-Driscoll J L, Jia Q X, Maiorov B, Wang H and Maley M 2007 *Nat. Mater.* **6** 631–642

[9] Puig T, Gutiérrez J, Pomar A, Llordés A, Gázquez J, Ricart S, Sandiumenge F and Obradors X 2008 *Supercond. Sci. Technol.* **21** 034008:1–12

[10] Foltyn S R, Civale L, MacManus-Driscoll J L, Jia Q X, Maiorov B, Wang H and Maley M 2011 299–310

[11] Haugan T J, Puig T, K M and Wu J 2019 *Supercond. Sci. Technol.* **33** 040301:1–5

[12] MacManus-Driscoll J and Wimbush S 2021 *Nat. Rev. Mater.* **6** 587:1–18

[13] Wu J and Shi J 2017 *Supercond. Sci. Technol.* **30** 103002:1–15

[14] Cantoni C, Gao Y, Wee S H, Specht E D, Gazquez J, Meng J, Pennycook S J and Goyal A 2011 *ACS Nano* **5** 4783–4789

[15] Paturi P, Malmivirta M, Hynninen T and Huhtinen H 2018 *J. Phys. Cond. Mat.* **30** 315902:1–7

[16] Kobayashi H, Yamada Y, Ibi A, Miyata S, Shiohara Y, Kato T and Hirayama T 2007 *Physica C* **463–465** 661–664

[17] Kang S, Leonard K J, Martin P M, Li J and Goyal A 2007 *Supercond. Sci. Technol.* **20** 11–15

[18] Ichinose A, Naoe K, Horide T, Matsumoto K, Kita R, Mukaida M, Yoshida Y and Horii S 2007 *Supercond. Sci. Technol.* **20** 1144–1150

[19] Liu Y and Du G 2011 *Journal of Electronic Materials* **40** 1512–1516

[20] Campbell T A, Haugan T J, Maartense I, Murphy J, Brunke L and Barnes P N 2005 *Physica C* **423** 1

[21] Matsumoto K, Tanaka I, Horide T, Mele P, Yoshida Y and Awaji S 2014 *J. Appl. Phys.* **116** 163903:1–7

[22] Malmivirta M, Rijckaert H, Paasonen V, Huhtinen H, Hynninen T, Jha R, Awana V S, Driessche I V and Paturi P 2017 *Sci. Reports* **7** 14682:1–8

[23] Aye M M, Rivasto E, Khan M Z, Rijckaert H, Palonen H, Huhtinen H, Van Driessche I and Paturi P 2021 *New J. Phys.* **23** 113031:1–12

[24] Mikheenko P, Abell J S, Sarkar A, Dang V S, Kechik M M A, Tanner J L, Paturi P, Huhtinen H, Babu N H, Cardwell D A and Crisan A 2010 *Journal of Physics: Conference Series* **234** 022022

[25] Yoshida Y, Miura S, Tsuchiya Y, Ichino Y, Awaji S, Matsumoto K and Ichinose A 2017 *Superconductor Science and Technology* **30** 104002

[26] Itoh M, Yoshida Y, Ichino Y, Miura M, Takai Y, Matsumoto K, Ichinose A, Mukaida M and Horii S 2004 *Physica C: Superconductivity* **412-414** 833–837

[27] Paranthaman M, Lee D F, Goyal A, Specht E D, Martin P M, Cui X, Mathis J E, Feenstra R, Christen D K and Kroeger D M 1999 *Supercond. Sci. Technol.* **12** 319–325

[28] Goyal A, Feenstra R, Paranthaman M, Thompson J R, Kang B Y, Cantoni C, Lee D F, List F A, Martin P M, Lara-Curzio E, Stevens C, Kroeger D M, Kowalewaski M, Specht E D, Aytug T, Sathyamurthy S, Williams R K and Erikson R E 2002 *Physica C* **382** 251–262

[29] Bhuyian M S, Paranthaman M, Kang S, Lee D F and Salama K 2005 *Physica C* **422** 95–101

[30] Li Z, Coll M, Mundet B, Chamorro N, Vallès F, Palau A, Gazquez J, Ricart S, Puig T and Obradors X 2019 *Sci. Rep.* **9** 5828

[31] Rivasto E, Hynninen T, Huhtinen H and Paturi P 2023 *J. Phys. Cond. Mat.* **35** 075701:1–10

[32] Rivasto E, Todorovic M, Huhtinen H and Paturi P 2023 *New Journal of Physics* **25** 113046:1–15

[33] Rivasto E, Aye M M, Huhtinen H and Paturi P 2024 *J. Phys. Cond. Mat.* **36** 135702:1–9

[34] Khan M Z, Rivasto E, Rijckaert H, Zhao Y, Liedke M O, Butterling M, Wagner A, Van Driessche I, Huhtinen H and Paturi P 2022 *Cryst. Growth Des.* **22** 2097–2104

[35] Aye M M, Rivasto E, Khan M Z, Rijckaert H, Salojärvi E, Haalisto C, Mäkilä E, Palonen H, Huhtinen H, Van Driessche I and Paturi P 2021 *Sci. Rep.* **11** 6010:1–11

[36] Khan M Z, Rivasto E, Rijckaert H, Zhao Y, Liedke M O, Butterling M, Wagner A, Van Driessche I, Huhtinen H and Paturi P 2022 *Cryst. Growth Des.* **22** 2097–2104

[37] Wiesinger H P, Sauerzopf F M and Weber H W 1992 *Physica C* **203** 121–128

[38] Cai C, Holzapfel B, Hänisch J, Fernandez L and Schultz L 2004 *Phys. Rev. B* **69** 104531:1–8

[39] Stangl A, Palau A, Deutscher G, Obradors X and Puig T 2021 *Sci. Rep.* **11** 8176:1–12

[40] Qin M J, Shi Z X, Ji H L, Ji X, Yao X X, Li H C and Rong X S 1995 *J. Appl. Phys.* **78** 3287–3292

[41] Varanasi C V, Barnes P N and Burke J 2007 *Supercond. Sci. Technol.* **20** 1071–1075

[42] Paturi P, Malmivirta M, Palonen H and Huhtinen H 2016 *IEEE T. Appl. Supercond.* **26** 8000705:1–5

[43] Paturi P and Huhtinen H 2022 *Supercond. Sci. Technol.* **35** 065007:1–9